ELSEVIER

High pressure-temperature phase relations of basaltic crust up to mid-mantle conditions

HPSTAR
1393-2022

Takayuki Ishii [a,b,*], Nobuyoshi Miyajima [b], Giacomo Criniti [b], Qingyang Hu [a], Konstantin Glazyrin [c], Tomoo Katsura [b]

[a] *Center for High Pressure Science and Technology Advanced Research, Beijing, 100094, China*
[b] *Bayerisches Geoinstitut, University of Bayreuth, Universitätsstraße 30, 95447 Bayreuth, Germany*
[c] *Deutsches Elektronen-Synchrotron DESY, Notkestr. 85, 22607 Hamburg, Germany*

ABSTRACT

A substantial amount of subducted basaltic crusts may exist in the lower mantle. It features distinct chemical composition from the peridotitic mantle and plays important roles in the chemical and dynamic evolution of Earth's interior. However, the chemical composition of mineral phases present in basaltic crust in the lower mantle is still poorly constrained. Here, we determined phase relations of normal mid-ocean ridge basalt (MORB) up to 52 GPa at 2000 K by multi-anvil press. Throughout our experiments, the mineral assemblages consist of five phases including bridgmanite, stishovite, calcium perovskite (davemaoite), calcium ferrite and new hexagonal aluminous phases. The density of MORB calculated from our phase assemblages and previously published thermoelastic data is 2-3% higher than that of the average mantle, which is consistent with literature. The new hexagonal aluminous phase is a host of potassium but only occupies 1-2 vol.% due to limited abundance of potassium in normal MORB. This indicates that the new hexagonal aluminous phase doesn't affect the elastic properties of basalt. Electron energy-loss spectra of recovered basaltic Al-rich bridgmanite show significant enrichment of ferrous iron (75-85%) compared with peridotitic Al-poor bridgmanite ($\sim$30%), which is against previous studies showing that ferric iron ratio in bridgmanite increases with Al content. Ferric iron exhibits strong partitioning into the new hexagonal aluminous phase (41-64%), whereas bridgmanite (14-28%) and calcium ferrite phase (5-27%) remain Fe^{2+}-enriched. The oxygen vacancy component of $MgAlO_{2.5}$ in bridgmanite is $\sim$11% up to 40 GPa, which is much higher than that in peridotitic bridgmanite (2-3%), possibly producing a viscosity contrast in the mid-mantle that would explain slab stagnation and plume thinning between 660 km and 1000 km depth. The presence of ferrous iron-rich bridgmanite in the deep lower mantle may contribute to seismic features of large low-shear-velocity provinces.

© 2022 Elsevier B.V. All rights reserved.

1. Introduction

Understanding the structure and dynamics of Earth's lower mantle that occupies the largest volume fraction of Earth's interior is of great importance for explaining the chemical, thermal and geodynamic evolutions of the Earth's interior. It is widely accepted that the upper mantle consists of peridotite, and therefore the lower mantle is naturally considered to have the same composition. Comparison of elastic properties and density of peridotite

with seismic observations support this hypothesis (e.g., Irifune et al., 2010; Kurnosov et al., 2017). Hereafter we assume that the average mantle composition is peridotitic.

Mid-ocean ridge basalt (MORB), of which the top layer of the subducting slab should be made, is compositionally different from peridotite. MORB is richer in Si, Fe, Al, Ca, Na, and K but poorer in Mg than peridotite. It is thus expected that subducted MORB plays an essential role in producing chemical heterogeneity and physical property variation in the mantle. Seismological studies using S-to-P converted waves have observed 7-km thick seismic scatterings in the lower mantle, for example, beneath the Izu-Bonin-Mariana arc (e.g., Kaneshima, 2019). Bentham et al. (2017) analyzed PP precursors by creating the global stacks and suggested that such small-scale seismic scatterings are randomly distributed throughout the

lower mantle. These small-scale heterogeneities are considered to be MORB bodies. Ballmer et al. (2015) proposed that the volume fraction of subducted basaltic crusts increases with depth in the lower mantle on the basis of numerical modeling. These studies suggested that the subducted basaltic crusts should exist in the lower mantle to affect mantle dynamics. Therefore, the mineral chemistry in the basaltic system under lower-mantle conditions is essential to discuss the lower-mantle structure and dynamics.

Many studies have investigated the phase relations of MORB under lower-mantle conditions (Irifune and Ringwood, 1993; Hirose et al., 1999; Ono et al., 2001; Litasov and Ohtani, 2005; Perrillat et al., 2006; Ricolleau et al., 2010; Ishii et al., 2019a). At the top of the lower mantle, a mineral assemblage of garnet + stishovite (St) + calcium perovskite (davemaoite, Dm) (Tschauner et al., 2020) is stable, and the density of MORB is lower than that of the average mantle. This assemblage transforms to bridgmanite (Brg) + St + Dm + Al-rich phases at 26-27 GPa, and its density becomes higher than the average mantle. Two Al-rich phases were reported. One of them is the calcium ferrite-structured phase with an orthorhombic unit cell (CF) and *Pnma* space group. This phase was initially reported as a decomposition product of garnet in a lower-mantle MORB by Irifune and Ringwood (1993). The other has a hexagonal unit cell and was thus called new-hexagonal-aluminous phase (NAL), formed from the decomposition of natural pyrope-almandine-grossular garnet by Miyajima et al. (1999). At higher pressures, the phase relations of MORB are poorly constrained. Ono et al. (2001) determined the phase relations of MORB up to 37 GPa using a multi-anvil press (MAP), showing that the proportion of NAL is close to zero while those of Brg, St, Dm, and CF remained the same with pressure. On the other hand, Ricolleau et al. (2010) employed laser-heated diamond anvil cell (LH-DAC) and observed that the proportion of NAL was 20 vol.% at the top of the lower mantle, although the fraction reduced with pressure and disappeared around 50 GPa, corresponding to 1000-1200 km depths. The proportion of Brg increased at the cost of NAL.

The discrepancy between previous phase relation studies makes the density contrast between the average mantle and MORB in the lower mantle unclear. Ono et al. (2001) suggested that a density crossover between MORB and Preliminary reference Earth model (PREM) (Dziewonski and Anderson, 1981) occurs in the mid-lower mantle (>~1400 km depth) on the basis of the extrapolation of low-pressure thermoelastic data. On the other hand, Ricolleau et al. (2010) suggested that MORB density is 1-3% higher than that of PREM at the lower mantle conditions.

The above mentioned discrepancy may stem from the difference in the adopted experimental methods. LH-DAC experiments by Ricolleau et al. (2010) may have produced a large temperature gradient which caused Fe-loss in the sample due to the Soret effect. As a result, their phase compositions disagreed with those obtained by MAP (Ono et al., 2001; Litasov and Ohtani, 2005; Ishii et al., 2019a) at top lower-mantle conditions. On the other hand, the pressure conditions of MAP studies were limited up to 37 GPa, and the compositions of phases couldn't be well constrained due to the small grain size of the recovered samples that made impossible the use of electron microprobe for analyses.

In this study, high-pressure-temperature phase relations of MORB were determined under lower mantle conditions up to 52 GPa at 2000 K employing our advanced multi-anvil technology (Ishii et al., 2016, 2017, 2019b) in combination with analytical transmission electron microscopy and synchrotron X-ray diffraction to analyze the recovered samples. We then discussed the lower-mantle structure and dynamics using our obtained phase relations, mineral chemistry, and estimated density.

2. Experimental method

2.1. Starting material

The starting material consisted of a finely ground oxide mixture. The nominal bulk composition is an average normal MORB, which is the same as the one reported by Ono and Yasuda (1996): SiO_2, 51.0; TiO_2, 1.7; Al_2O_3, 15.7; FeO, 9.9; MgO, 7.7; CaO, 11.2; Na_2O, 2.4; K_2O, 0.2 in wt.%. Reagent grade Fe_2O_3, $CaCO_3$, Na_2CO_3, and K_2CO_3 were used as sources of FeO, CaO, Na_2O, and K_2O, respectively. All samples were dried in a furnace before weighing to remove adhesive water. SiO_2 and MgO were heated at 1273 K for 12 h, and TiO_2, Al_2O_3, and Fe_2O_3 were at 773 K for 12 h. $CaCO_3$, Na_2CO_3, and K_2CO_3 were dried at 423 K for 24 h. These oxides and carbonates were ground for 1 h in an agate mortar. The mixture was melted at 1873 K for 1 h and quenched by dropping into water. The quenched product was ground with an agate mortar for 1 h. The powdered sample was then heated at 1273 K for 24 h in a $CO-CO_2$ gas mixing furnace controlled at a P_{O_2} of approximately 1 log unit above the iron-wüstite buffer to make iron valence in the sample ferrous. Afterwards, the treated sample was ground again for 1 h.

To estimate the pressure generation in each run, the Al_2O_3 contents in bridgmanite in the $MgSiO_3$-Al_2O_3 system was used (Liu et al., 2017a). The starting material for the pressure calibrant was placed next to the MORB starting material in a high-pressure cell assembly (Fig. S1). The starting material of this calibrant was prepared as akimotoite with compositions of $MgSiO_3$:Al_2O_3 = 81.25:18.75, 75:25 and 65:35 in moles. Regent MgO, SiO_2, and Al_2O_3 were mixed and ground in an agate mortar for 1 h. The mixtures were then heated at 1923 K for 1 h and dropped in water to be quenched to glasses. The quenched glasses were ground again and then converted into akimotoite at 25 GPa and 1073 K for 1 h using a multi-anvil press (Ishii et al., 2016).

2.2. High pressure-temperature experiment

High-pressure experiments were conducted at pressures from 27 to 52 GPa and a temperature of 2000 K for 2-3 h using the Kawai-type multi-anvil press with the Osugi (DIA) module installed at the Bayerisches Geoinstitut, University of Bayreuth (IRIS-15) (Ishii et al., 2016, 2019b). Experiments at 27-45 GPa were performed using TF05-grade tungsten carbide anvils, whereas the run at 52 GPa was conducted using TJS01-grade tungsten carbide anvils, which are harder than TF05 grade (Ishii et al., 2017). As mentioned above, the sample pressures were estimated based on the alumina content in bridgmanite (Liu et al., 2017a) with an uncertainty of 0.4-0.9 GPa, as shown in Table 1. We used two kinds of high-pressure cell assembly (Fig. S1). Tungsten carbide anvils with truncated edge lengths of 3.0 and 1.5 mm, respectively, were combined with a Cr-doped magnesia pressure medium with edge lengths of 7.0 and 5.7 mm to generate a pressure of 27 GPa or higher, respectively. For experiments at 40, 45, and 52 GPa, we used tapered anvils with 1° slopes (Ishii et al., 2016, 2017, 2019b). A Re cylindrical foil was used as a heater. A ZrO_2 sleeve was adopted around the heater as a thermal insulator. Mo electrodes connected both ends of the heater to anvils. The MORB sample and pressure calibrant were directly loaded into the heater. Re disks with a thickness of 25 μm were placed between the sample, pressure calibrant and Al_2O_3 lids to avoid reactions among them. A W-3%Re/W-25%Re thermocouple was set on the surface of the central part of the heater to monitor the sample temperature.

The sample was compressed to a desired press load and was then heated to the target temperature. After heating for 2-3 hours, it was quenched by shutting off the electric supply to the heater.

Table 1
Experimental conditions, phase assemblage, and mineral proportions.

Run No.	P† GPa	T K	D h	Calibrant composition¶	Brg calibrant composition§	Phase assemblage (proportion, vol.%)	‡Density g/cm³
1882	27.1(5)	2000	3	$En_{81.25}Cor_{18.75}$	$Mg_{3.51(3)}Al_{1.00(3)}Si_{3.50(2)}O_{12}$	Brg(24)+St(24)+Dm(24)+CF(26)+NAl(2)	4.53
1914	35.1(7)	2000	3	$En_{81.25}Cor_{18.75}$	$Mg_{3.27(2)}Al_{1.45(4)}Si_{3.28(3)}O_{12}$	Brg(27)+St(23)+Dm(24)+CF(25)+NAl(1)	4.63
1978	39.9(9)	2000	3	$En_{75}Cor_{25}$	$Mg_{3.15(4)}Al_{1.72(5)}Si_{3.14(4)}O_{12}$	Brg(30)+St(20)+Dm(23)+CF(26)+NAl(1)	4.67
1588	44.7(4)	2000	3	$En_{75}Cor_{25}$	$Mg_{2.99(2)}Al_{1.99(2)}Si_{3.01(2)}O_{12}$	Brg(31)+St(21)+Dm(20)+CF(26)+NAl(2)+Fe*	4.75
1975	52.4(9)	2000	2	$En_{65}Cor_{35}$	$Mg_{2.80(4)}Al_{2.42(5)}Si_{2.79(3)}O_{12}$	Brg(32)+St(22)+Dm(22)+CF(22)+NAl(2)	4.87

† Pressures were estimated from alumina contents of the calibrants. Number in parentheses represents pressure uncertainties for the last digit based on compositional errors of aluminous bridgmanite.

¶ Compositions of starting materials for the calibrants.

§ Compositions of aluminous bridgmanites in the calibrants, in which the data for 1975 was determined by TEM-EDS and others were by EPMA.

*Fe metal was observed but was not included in the mass balance calculation.

‡ Densities calculated at given pressure-temperature conditions in this table (see text for details).

En, enstatite; Cor, corundum; Brg, bridgmanite; Dm, davemaoite (calcium perovskite); St, stishovite; CF, calcium ferrite; NAl, new-hexagonal-aluminous phase.

Sample pressure was finally decreased to the atmospheric pressure in 12-15 hours at room temperature.

2.3. Analyses of run products

Recovered samples were mounted in epoxy resin and polished for textual observation by micro-focused X-ray diffraction (XRD) and scanning electron microscopy. The XRD was conducted for initial phase identification using a micro-focused X-ray diffractometer (Bruker, D8 DISCOVER) with a two-dimensional solid-state detector (VÅNTEC500) at the Bayerisches Geoinstitut. A micro-focus source (IμS) of Co-Kα radiation, which was focused to 50 μm beam using a IFG polycapillary X-ray mini-lens, was operated at 40 kV and 500 μA. The scanning electron microscopy was conducted using a LEO1530 scanning electron microscope (SEM) with an energy-dispersive X-ray spectrometer (EDS) operated at an acceleration voltage of 10-15 kV and a beam current of 10 nA. Compositional analysis for the pressure calibrants of aluminous bridgmanite was carried out using an electron microprobe (EPMA) with wavelength-dispersive spectrometers (JEOL, JXA-8200) and an acceleration voltage and probe current of 10 kV and 5 nA, respectively. Synthetic enstatite for Mg and Si and corundum for Al were used as standard materials.

Chemical compositions of the recovered samples were determined by transmission electron microscopy (TEM). Thin sections of the recovered samples were prepared using a Ga$^+$ focused ion beam (FIB) instrument (FEI, Scios Dual Beam). One or two 10 μm × 20 μm thin sections of the recovered sample at each condition were cut out by FIB. The samples were thinned to approximately 80-nm thickness using Ga$^+$ ion beams. The sample lamellae were analyzed using an FEI Titan G2 80–200 S/TEM transmission electron microscope operated at 200 keV and equipped with a Gatan GIF Quantum SE EELS system and a Bruker Quantax energy-dispersive X-ray spectrometer (EDXS). The chemical compositions of constituent phases were determined with an off-line evaluation on EDXS spectrum imaging data (i.e., chemical maps of each run products). Extracted spectra on each phase were evaluated with experimentally determined k-factor and an absorption correction. We measured 5-20 grains. The analytical errors were estimated by one standard deviation of the mean of these measurements. Ferric iron ratios in the phases were determined by electron energy-loss spectroscopy (EELS). The evaluations of spectra in EDXS and EELS were performed, following the procedure described by Miyajima et al. (2004). The ferric iron ratios of Brg, CF, and NAL, respectively, were estimated by averaging ferric iron ratios of 5-8, 3-7, and 2-4 grains, in which the analytical errors were estimated by one standard deviation of the mean. Note that only one reliable ferric iron ratio was obtained for NAL at 45 GP and 52 GPa due to difficulty in finding NAL grains.

We note that we examined possible chemical heterogeneity in the sample synthesized at 45 GPa by comparing the proportions and compositions of the phases present in regions near the center and both ends. As mentioned later, the grain sizes decrease with increasing pressure, suggesting that the element diffusivity of the phases decreases with increasing pressure. Therefore, we can consider that all products may be homogeneous if the sample at 45 GPa is homogeneous. Actually, the phase proportions were identical, and their compositions were also identical within the errors.

After 10-24 months from the synthesis experiments and post-analysis mentioned above, synchrotron powder XRD was conducted at the Extreme Conditions Beamline P02.2 of Petra III (DESY, Hamburg, Germany) using 25.6 keV X-ray beams with horizontal and vertical widths of approx. 8 and 2 μm, respectively, and a Perkin Elmer flat panel detector. Polycrystalline CeO_2 was used to calibrate the sample-detector distance and the detector param-

eters. Fragments with a maximum dimension of 20-50 μm were hand-picked from each sample and placed on the culet of a diamond anvil (Fig. S2). The samples to the X-ray beam were aligned by collecting absorption profiles of a 20 μm W piece placed on the diamond culet next to the sample fragments. In this way, we moved the DAC using the W position as a reference and the pre-programmed positions of the five MORB pieces to take their individual XRD patterns without changing the holder or alignment. We thus reduced any potential error arising from different alignments of the fragments if they had been placed on separate holders. Two-dimensional XRD patterns were taken by oscillating the DAC in a range of ±15°. The accumulation time was 30 s for each sample to ensure that the intensity of Bragg's reflection was optimized for phase identification without saturating the detector. The two-dimensional diffraction patterns were then integrated into one-dimensional patterns using *DIOPTAS* software (Prescher and Prakapenka, 2015). The one-dimensional diffraction patterns were analyzed using the *Jana*2006 software (Petříček et al., 2014). After identifying the recovered phases, their lattice parameters were obtained using Le Bail refinements of full patterns employing manual background subtraction and pseudo-Voigt line shapes. Errors on the cell parameters were evaluated by following the Bérar and Lelann (1991) method, which took into account of the potential correlation between intensities of neighboring data points.

2.4. Density calculation

The densities of MORB at high-pressure-temperature conditions were calculated in the following procedure. The volumes of MORB constituent minerals at high pressure and high temperature were calculated by the third-order high-temperature Birch-Murnaghan equation of state expressed as

$$P = \frac{3}{2} K_{T,0} \left[\left(\frac{V_{T,0}}{V_{T,P}} \right)^{\frac{7}{3}} - \left(\frac{V_{T,0}}{V_{T,P}} \right)^{\frac{5}{3}} \right]$$
$$\times \left[1 + \frac{3}{4} \left(K'_{T,0} - 4 \right) \left\{ \left(\frac{V_{T,0}}{V_{T,P}} \right)^{\frac{2}{3}} - 1 \right\} \right] \tag{1}$$

where $V_{T,0}$ and $V_{T,P}$ are the molar volumes at T at 1 atm and P, respectively, $K_{T,0}$ is the isothermal bulk modulus at T, and $K'_{T,0}$ is the pressure derivative of $K_{T,0}$. For temperature effects:

$$K_{T,0} = K_0 + \left(\frac{\partial K_{T,0}}{\partial T} \right)_P (T - 298) \tag{2}$$

where K_0 is the isothermal bulk modulus at 298 K and 1 atm. The temperature effect on the volume of each mineral was calculated using its thermal expansivity.

$$V_{T,0} = V_0 exp \int_{298}^{T} \alpha_{T,0} dT \tag{3}$$

$$\alpha_{T,0} = \alpha_0 + \alpha_1 T \tag{4}$$

where V_0 is the volume at 298 K and 1 atm and $\alpha_{T,0}$ is the thermal expansivity at T and ambient pressure. Table 2 summarizes the thermoelastic parameters of minerals used for the high-pressure-temperature volume calculation. We adopted the thermoelastic properties of phases with compositions close to the compositional data obtained in this study. The thermoelastic parameters of $CaSiO_3$ and SiO_2 end-members were used for Dm and St, respectively.

3. Results and discussion

3.1. Phases present

At room pressure and temperature, five phases were identified from the XRD patterns of the quenched run products: bridgmanite (Brg) with orthorhombic perovskite-type structure, stishovite (St) with tetragonal rutile-type structure, calcium ferrite-type aluminous phase (CF) with orthorhombic symmetry, the new-hexagonal aluminous-phase (NAL) with hexagonal symmetry, and $CaSiO_3$ perovskite (Davemaoite, Dm) with cubic perovskite-type structure (Figs. 1, S3-5). The SEM-EDS and TEM-EDS analyses confirmed these five phases coexist in all samples (Fig. 2). The phases with almost pure SiO_2 compositions, Ca-rich compositions, and Mg-rich compositions, respectively, were identified as St, Dm, and Brg (Fig. 2f). We found potassium-rich and -free Al-rich grains (Fig. 2f) were associated with NAL and CF, respectively, because potassium is known to strongly partition into NAL despite the similarity of the other components between these two phases (Miyajima et al., 2001). It is also noted that the Na content in CF is significantly higher than that in NAL, indicating that Na is strongly partitioned into CF. The run at 45 GPa exhibited an additional phase, which had a high brightness in back-scattered electron (BSE) images and contained pure iron, and was thus identified as metallic iron (Fig. 2e). The presence of the five oxide phases observed in this study generally agrees with the results of previous reports (Hirose and Fei, 2002; Perrillat et al., 2006; Ricolleau et al., 2010; Ishii et al., 2019a). Compositions of these phases are summarized in Table S1.

As mentioned in the introduction, the stability and abundance of NAL have been under debate over the last two decades (Ono et al., 2001; Litasov and Ohtani, 2005; Perrillat et al., 2006; Ricolleau et al., 2010; Ishii et al., 2019a). The MAP study of Ono et al. (2001) reported that NAL was absent in their investigated pressure range, i.e., up to 37 GPa. One possibility for this discrepancy from the current study is that only tiny amounts of NAL were present in their run product, and therefore SEM could not detect it due to the limited spatial resolution. The DAC studies, on the other hand, reported that the stability field of NAL extends up to ~50 GPa (Perrillat et al., 2006; Ricolleau et al., 2010). Perrillat et al. (2006) identified NAL by X-ray diffraction. Ricolleau et al. (2010) conducted runs at 44 GPa and 55 GPa, and phase identifications carried out by X-ray diffraction and TEM-EDS showed that NAL is still present at 44 GPa, but disappears at 55 GPa. Our X-ray diffraction patterns on the recovered samples showed very weak NAL peaks (2 theta = ~3.65° corresponding to d = ~7.60 Å) below 40 GPa, and became even weaker above 45 GPa (Fig. 1). However, our TEM-EDS images unambiguously recognized the presence of NAL at 45 and 52 GPa, concluding that the stability of NAL extends up to at least 52 GPa. Although NAL could disappear at a pressure between 52 GPa and 55 GPa, this is unlikely because the volume fraction of NAL seemed stable with pressure (Table 1 and see the section 3.3 below).

We observed weak diffraction peaks of Dm in all runs (Fig. 1), which had been considered unquenchable. The composition of Dm is close to $CaSiO_3$, although small amounts of MgO (0.52-1.77 wt.%), Al_2O_3 (0.5-5.3 wt.%), TiO_2 (0.93-1.9 wt.%) and FeO (1.3-4.9 wt.%) were detected, consistently with previous observations (Table S1a). In contrast to the previous studies (Irifune and Ringwood, 1993; Ono et al., 2001; Hirose and Fei, 2002; Hirose et al., 2005; Ricolleau et al., 2010; Ishii et al., 2019a), Dm was found recoverable to ambient conditions and confirmed by synchrotron X-ray diffraction. The reason for the recoverability in this study is unknown. Although the diffraction signal of Dm was weak in all samples, that at 27 GPa was particularly weak (Fig. S3). Therefore, we speculate that the synthesis at higher pressure may enhance

Table 2
Volumes at ambient pressure from XRD analyses and thermoelastic parameters of the identified phases.

Phase		Dm	Brg	St	CF	NAL
V (52 GPa)	Å^3	45.3(1)[a]	168.5(3)	46.64(4)	243.3(4)	185.94[e]
V (45 GPa)	Å^3	45.4(1)[a]	169.3(5)	46.65(3)	243.3(3)	185.94[e]
V (40 GPa)	Å^3	45.5(2)[a]	168.41(2)	46.60(4)	243.8(5)	185.94[e]
V (35 GPa)	Å^3	46.0(1)[a]	169.4(2)	46.60(3)	243.9(4)	185.94[e]
V (27 GPa)	Å^3	46.0(2)[a]	169.4(2)	46.66(3)	244.5(2)	185.94[e]
K_0	GPa	248[b]	239[c]	296[d]	174[c]	198[e]
$K'_{T,0}$		4.2[b]	3.98[c]	4.2[d]	4.86[c]	5.1[f]
$(\partial K_{T,0}/\partial T)_P$	GPa·K^{-1}	−0.036[b]	−0.04[c]	−0.046[d]	−0.013[c]	−0.016[f]
$\alpha_0 \times 10^5$	K^{-1}	2.00[b]	2.83[c]	1.26[d]	2.56[c]	3.44[f]
$\alpha_1 \times 10^8$	K^{-2}	1.90[b]	1.62[c]	1.29[d]	0.00[c]	0.10[f]

Abbreviations: Brg, bridgmanite; Dm, CaSiO$_3$-rich perovskite; St, stishovite; CF, NaAlSiO$_4$-rich calcium ferrite; NAL, new-hexagonal-aluminous phase.
a, Calculated as cubic structure; b, Gréaux et al. (2019); c, Ricolleau et al. (2010); d, Nishihara et al. (2005); e, Ono et al. (2002); f, Shinmei et al. (2005).
Volumes were estimated from X-ray diffraction profiles of recovered samples (Fig. 1).
Thermal expansivity is expressed as $\alpha_{T,0} = \alpha_0 + \alpha_1 T$.
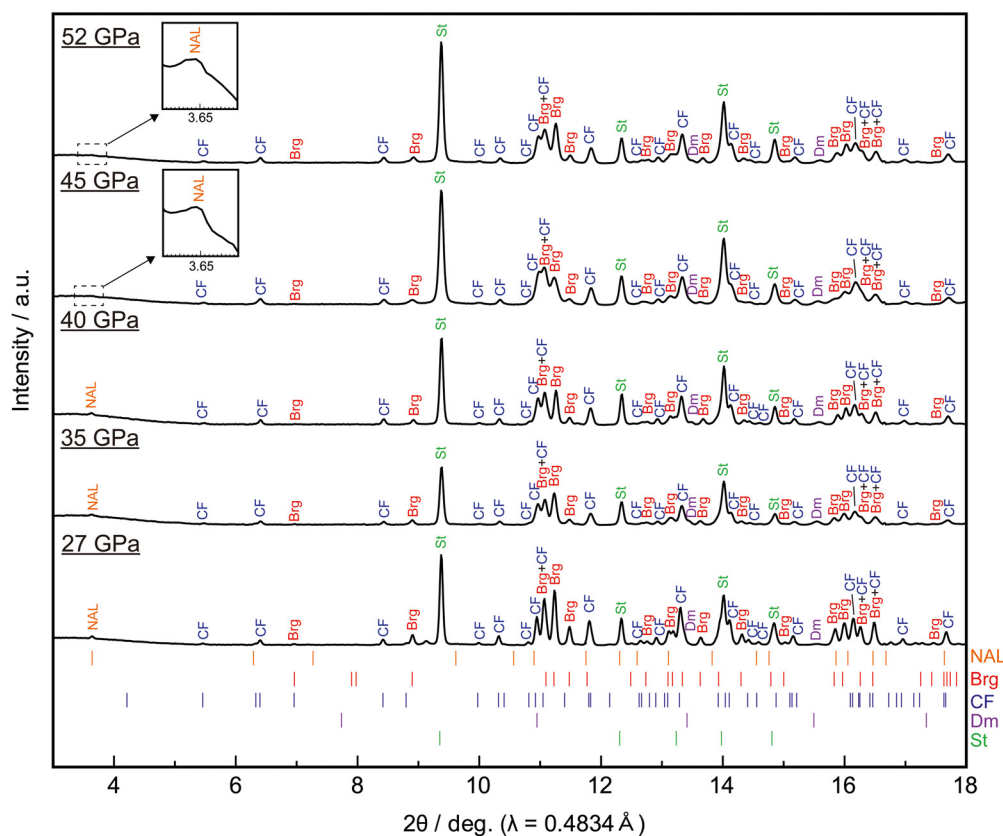
Fig. 1. Synchrotron powder X-ray diffraction patterns of samples recovered from 27-52 GPa. Tick marks are diffraction positions of each phase calculated for the 27 GPa profile. Peak positions of NAL were calculated with lattice parameters of NAL reported by Ono et al. (2002). We observed only the 100 peak for NAL, which has the strongest intensity. Brg, bridgmanite; CF, calcium ferrite; NAL, new-hexagonal-aluminous phase; Dm, calcium perovskite; St, stishovite.

recoverability. The reason for the unrecoverability of Dm in the previous DAC experiments may be due to bad crystallinity under the large deviatoric stresses and heterogeneous temperature fields. Note that we did not observe any Dm electron diffraction by TEM in contrast to X-ray diffraction, probably because quenched Dm was amorphized by the Ga ion beam during FIB cutting and intense electron beam during TEM observation. The use of well-sintered samples with nanosized crystallites may also have helped preserve the structure of Dm in the inner part of the samples due to possible residual strain arising from intergrain interactions. The measured volumes at ambient conditions (45.3-46.0 Å^3) agree with previously estimated ones from the compression experiments (~45.6 Å^3) (Hirose et al., 2005; Ricolleau et al., 2010). It was reported that St transforms to a CaCl$_2$-type phase at mid-lower mantle pressures by a second-order transition, with the transition

pressure decreasing with increasing Al$_2$O$_3$ content (Lakshtanov et al., 2007). Ricolleau et al. (2010) observed the transition in silica with less than 1 wt.% of Al$_2$O$_3$ at 55 GPa and 300 K. Hirose et al. (2005) showed stishovite is stable at 56.4-60.8 GPa and 1890-2140 K. St in the present study also has similar amounts of alumina (0.6-1.0 wt.%). It is therefore reasonable to assume that St is the stable polymorph of SiO$_2$ at our experimental conditions.

The presence of metallic iron suggests that charge disproportionation of ferrous iron (Frost et al., 2004) took place in the run at 45 GPa, constituting the first observation of iron disproportionation in basaltic systems. However, as mentioned below, not only Brg, but also CF and NAL contain Fe^{3+}. Therefore, iron was disproportionated not only by Brg, as in the case of peridotitic systems, but also by CF and NAL. No metallic iron was found in the samples from the other runs. We nevertheless consider that the
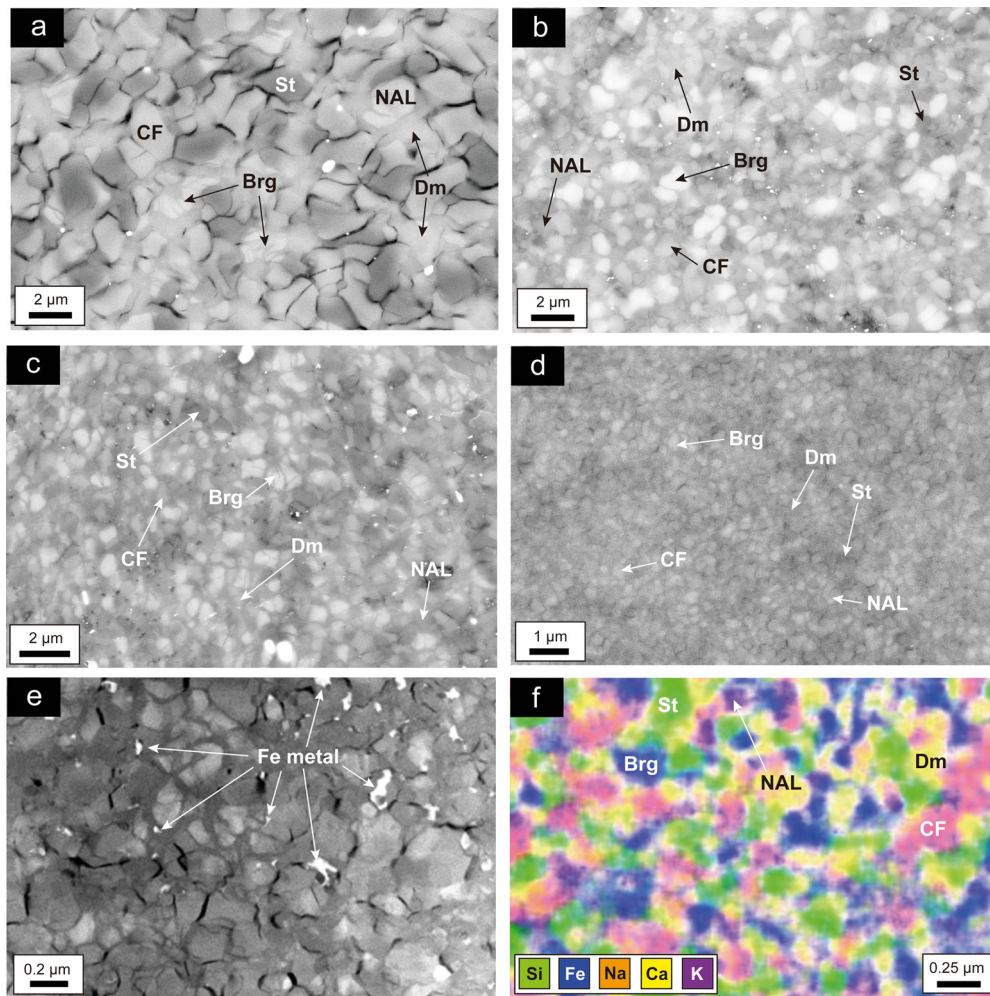
Fig. 2. Representative SEM-BSE images of the recovered samples at (a) 27, (b) 35 GPa, (c) 45 GPa, and (d) 52 GPa. (e) A STEM-HAADF image of the sample recovered from 45 GPa revealing the presence of Fe metal. (f) A STEM-EDS compositional map of the recovered sample at 52 GPa. Bright particles observed in (a)-(c) are Re metal attached during mechanical polishing. Brg, bridgmanite; CF, calcium ferrite; NAL, new-hexagonal aluminous-phase; Dm, calcium perovskite; St, stishovite.
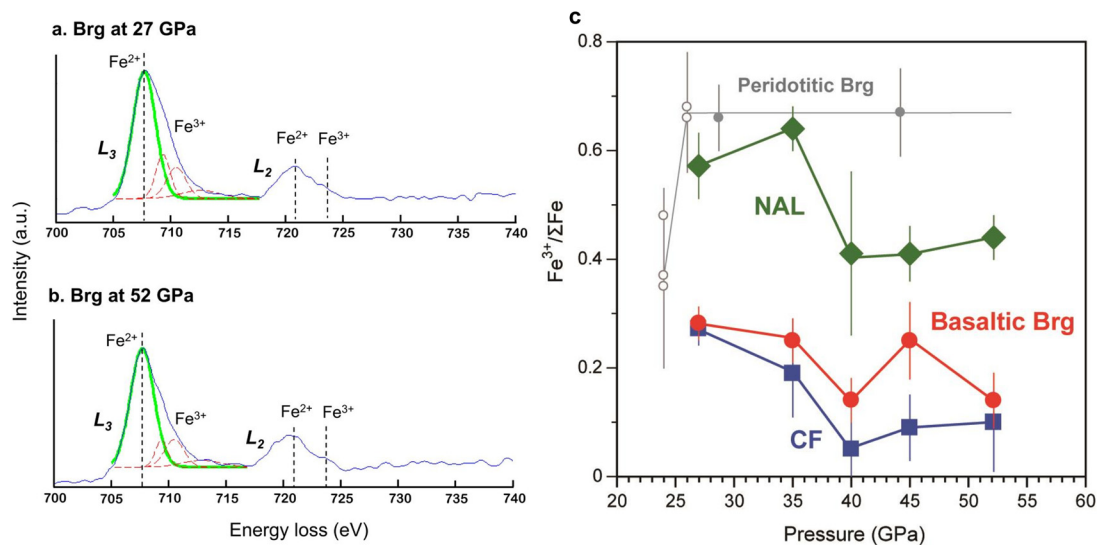

Fig. 3. Ferric iron ratios in basaltic bridgmanite (Brg), calcium ferrite phase (CF) and new-hexagonal-aluminous phase (NAL). (a,b) Representative EELS spectra of bridgmanite at 27 and 52 GPa, respectively. The intensity ratio of the green peak to the other three red peaks in the Fe L_3-edge was calibrated with $Fe^{3+}/\Sigma Fe$ values (van Aken and Liebscher, 2002). (c) Ferric iron ratios of the phases. Gray open and solid circles are data for peridotitic bridgmanite from Frost et al. (2004) and Irifune et al. (2010), respectively. (For interpretation of the colors in the figure(s), the reader is referred to the web version of this article.)
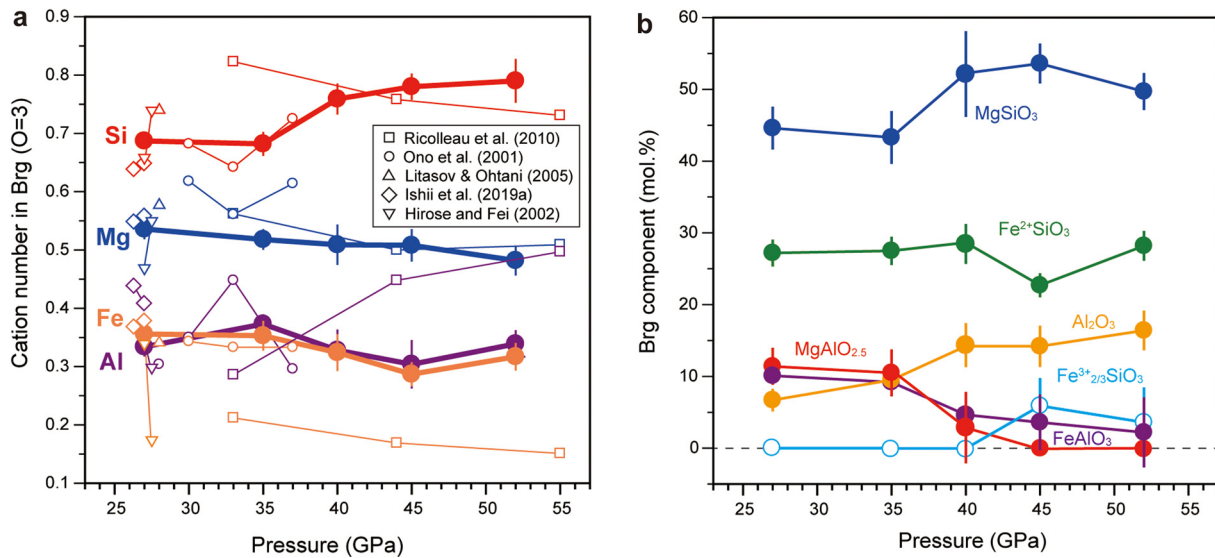
Fig. 4. Compositional change of bridgmanite with pressure. (a) cation number at the oxygen number of three. (b) Components in Brg.

disproportionation should have occurred in all runs because EELS spectroscopy detected ferric iron in Brg, CF, and NAL (Fig. 3). The reason for no detection of Fe metal in the other samples may be that the precipitated Fe metal was oxidized by small amounts of adhesive water and incorporated into oxide phases, although the starting materials were prepared in the same way. Note that a recent study indicates that the extent of disproportionation depends on Al and Fe contents in Brg, oxygen fugacity, and temperature (Huang et al., 2021), implying that further study is needed to clarify this phenomenon.

3.2. Chemical compositions of bridgmanite, calcium ferrite and new-hexagonal-aluminous phase

Fig. 3 shows the results of EELS measurements for Brg, CF, and NAL. The chemical compositions of each phase at each pressure are summarized in Table S1.

3.2.1. Bridgmanite

In general, Brg has 0.48-0.54 Mg, 0.33-0.37 Al, 0.69-0.79 Si, and 0.29-0.36 Fe in the formula with three oxygen. The $Fe^{3+}/\Sigma Fe$ in basaltic Brg is much smaller (0.14-0.28) than peridotitic Brg ($\sim$0.7) (Frost et al., 2004; Irifune et al., 2010).

Fig. 4 shows compositional changes in Brg with pressure. Mg decreases, whereas Si increases with pressure. Both Fe and Al decrease up to 45 GPa and increase again at 52 GPa. Our results generally agree with the previous MAP studies (Ono et al., 2001; Hirose and Fei, 2002; Litasov and Ohtani, 2005; Ishii et al., 2019a), but less agree with the DAC study (Ricolleau et al., 2010), especially in Fe and Al. Ono et al. (2001) determined the mineral compositions of the MAP samples by EPMA but mentioned that the grains were not always large enough to conduct good analysis. Since we observed that the grain size decreases from 2-3 to 0.2 μm with increasing pressure (Fig. 2), we imagine that Brg grains measured by Ono et al. (2001) may have been smaller than 1 μm, as shown in Fig. 1b, at 33 and 37 GPa. This may be the reason for the discrepancy in Brg compositions above 30 GPa between the present and their studies. The Brg compositions reported by Ricolleau et al. (2010) significantly differ from our results, showing lower Fe and higher Al contents than those reported in this study (Fig. 4a). They suggested that the large thermal gradient generated by the laser heating had caused 14-38% iron loss due to the Soret effect at 33-55 GPa, which should be the reason for the lower Fe content. As a consequence, the concentration of Al in the analyzed

area might have also increased. The compositional data at 27-27.5 GPa reported by Hirose and Fei (2002) significantly differ from our and other multi-anvil data. This discrepancy may be due to their higher experimental temperatures (2500-2720 K). Their sample at 27 GPa showed the presence of majorite coexisting with the five phases of CF, Dm, St, NAL, and Brg. The sample at 27.5 GPa showed coexistence of melt and (Al,Ca)-rich phase called CAS phase with Dm, St, NAL, and Brg. The presence of majorite, melt, and CAS phase would have led to different compositions of the five phases constituting the MORB system.

Fig. 4b shows the component changes with pressure by following the method described by Liu et al. (2020). The major components of Brg are firstly $MgSiO_3$ and, secondly, $FeSiO_3$. The $MgSiO_3$ component increases from 45 to 50 mol.% as pressure increases from 27 to 52 GPa. On the other hand, the $FeSiO_3$ component essentially remains unchanged. The Al_2O_3 component increases from 7 to 16 mol.% but does not monotonically change with pressure (Fig. 4a). The Al content in Brg increases with pressure when coexisting with corundum due to the larger partial volume of Al_2O_3 in corundum than Brg (Liu et al., 2017a). On the other hand, when Brg coexists with CF, the Al content in Brg essentially remains unchanged because CF has a similar density with Brg. As shown in Fig. 4b, although the Al_2O_3 component slightly increases, the $MgAlO_{2.5}$ and $FeAlO_3$ components decrease from 11 to 0 mol.% and from 10 to 2 mol.%, respectively. The relatively constant Al_2O_3 content with pressure shown in Fig. 4a is due to the trade-off of these changes. In our study, Brg contains large amounts of the oxygen vacancy component $MgAlO_{2.5}$ ($\sim$11 mol.%), which is much more abundant than that in peridotitic Brg (2-4 mol.%) (Frost et al., 2004; Irifune et al., 2010), at relatively low pressures of 27 and 35 GPa. This result disagrees with Liu et al. (2019), who demonstrated that the $MgAlO_{2.5}$ component appeared only when MgO is saturated in the bulk composition. Thus, this is probably because of the effect of Fe^{2+}, namely presence of $Fe^{2+}AlO_{2.5}$ component. This $MgAlO_{2.5}$ component was not observed above 40 GPa as mentioned above (Fig. 4b). The disappearance of the oxygen vacancy component with pressure agrees with Liu et al.'s (2017b) results. In contrast to the disappearance of the $MgAlO_{2.5}$ component, the cation vacancy component of $Fe^{3+}_{2/3}SiO_3$ seems to appear above 40 GPa, although the analytical errors hamper a definite conclusion.

Fig. 5a shows the relations between the Fe^{3+} ratio and Al content in Brg. The Fe^{3+} ratio seems to increase up to $\sim$80% with
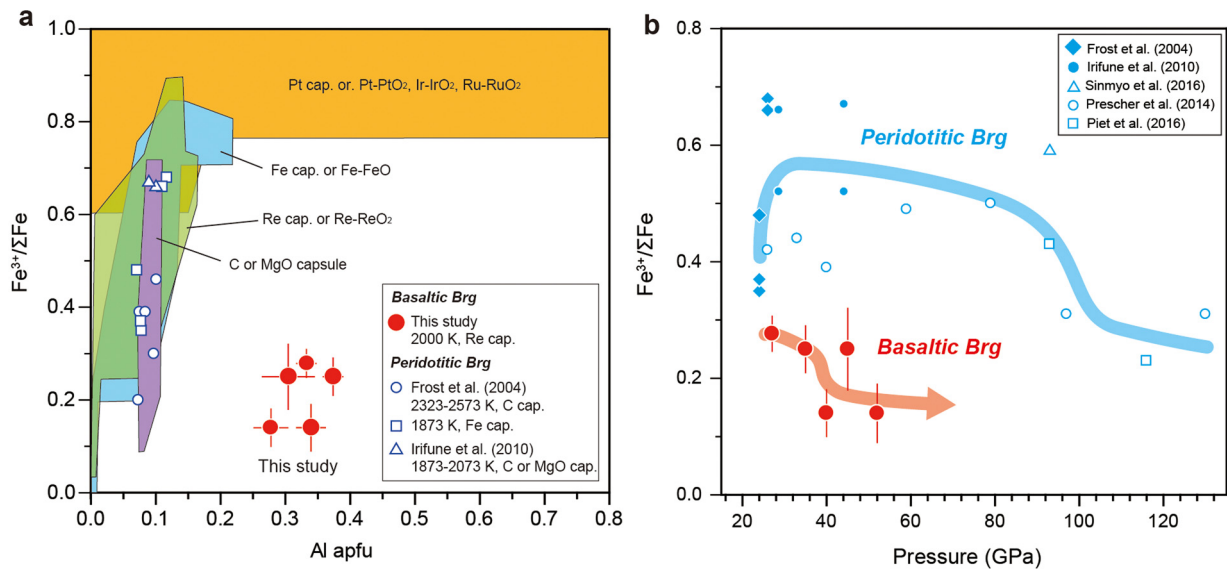
Fig. 5. Ferric iron ratio in bridgmanite as a function of (a) Al content and (b) pressure. Blue data points in (b) are bridgmanites in peridotite and pyrolite. The Al content was calculated assuming the cation number is 2.
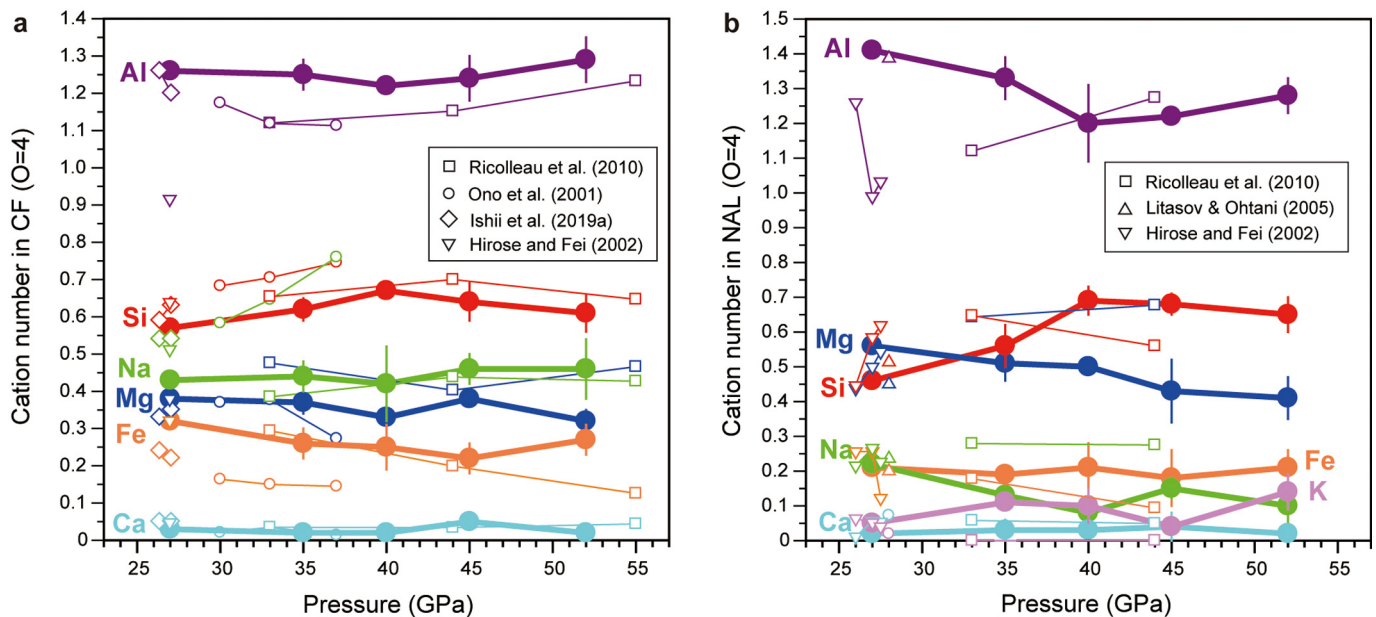

Fig. 6. Compositional changes of (a) calcium ferrite and (b) new-hexagonal-aluminous phases with pressure.

increasing Al content up to ~0.2 apfu when oxygen fugacity is at the Re-ReO$_2$ buffer (~IW+6) or less. On the other hand, Brg can accommodate 100% ferric iron when the oxygen fugacity is higher than the Re-ReO$_2$ buffer, such as the Pt-PtO$_2$ buffer (~IW+19). This figure indicates that ferric iron ratio in Brg increases with increasing Al content, except for extremely high oxygen fugacity conditions such as Pt-PtO$_2$ buffer. This trend has been generally accepted, as was suggested by Frost et al. (2004). On the other hand, the Fe^{3+} ratio in our Brg falls between 14 and 28% in spite of Al contents as large as 0.3-0.4 apfu, which is far from the trend of the previous studies. This result is opposite to the previous understanding as mentioned above. Thus, the crystal chemistry of basaltic Brg appears to be very different from that of peridotitic Brg. Fig. 5b shows the pressure dependence of the Fe^{3+} ratio in Brg. The Fe^{3+} ratio in Brg in MORB seems to decrease with pressure and to be lower than that of the peridotitic Brg in the entire

lower mantle pressure range (Frost et al., 2004; Irifune et al., 2010; Sinmyo et al., 2011; Prescher et al., 2014; Piet et al., 2016).

3.2.2. Calcium ferrite and new-hexagonal-aluminous phases

The CF composition is mainly described by the NaAlSiO$_4$-(Mg,Fe)Al$_2$O$_4$-Fe$_3$O$_4$-(Mg,Fe)$_2$SiO$_4$ system and our results suggest it has only minor change up to 52 GPa (Fig. 6a and Table S1), which is consistent with previous studies. Although NaAlSiO$_4$, (Mg,Fe)Al$_2$O$_4$, and (Mg,Fe)$_2$SiO$_4$ components are kept almost constant (45-50, ~40 and ~10 mol%, respectively), the Fe$_3$O$_4$ component decreased from ~10 to 1 mol.% with pressure due to the decrease of the ferric iron content in CF with pressure.

The NAL composition slightly changes at 40-45 GPa, especially in Al and Si (Fig. 6b). In general, NAL has three non-equivalent sites (nine-fold A, bicapped prism B and octahedral C sites) described as $A_{0.33}B_{0.67}C_2O_4$ (A = Na, K, Ca, B = Mg, Fe^{2+}, C = Al, Si, Fe^{3+}). At 27 GPa, the composition of NAL is expressed as (K,Na,Ca)$_{0.33}$(Mg,Fe^{2+})$_{0.67}$(Al,Si,Fe^{3+})$_2$O$_4$, similar to lit-
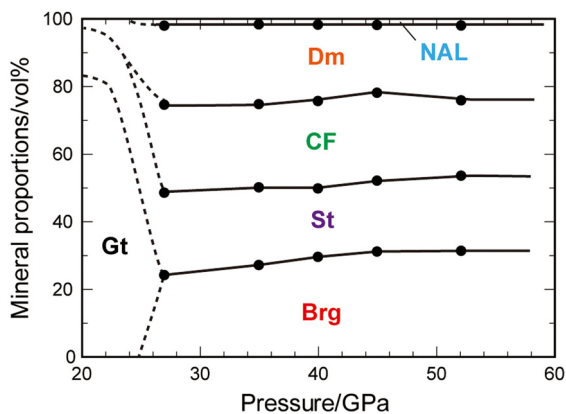
Fig. 7. Volume fractions of phases of MORB down to mid-mantle conditions. Dashed lines are drawn with data of Ishii et al. (2019a). Brg, bridgmanite; CF, calcium ferrite; NAL, new-hexagonal-aluminous phase; Dm, calcium perovskite; St, stishovite.
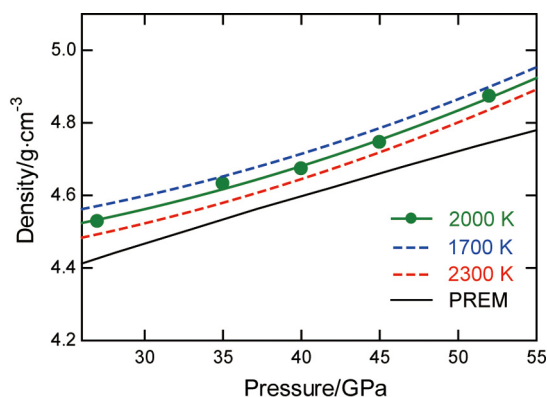

Fig. 8. Density of MORB in the lower mantle. Green data points are calculated from the present unit cell volumes and volume fractions of phases (see Table 1 and 2). Densities at 1700 and 2300 K were calculated using volume fractions of phases at 2000 K.

erature (Gasparik et al., 2000; Miyajima et al., 2001). On the other hand, at higher pressure it becomes $(K,Na,Ca)_{0.33}(Mg,Fe^{2+})_{0.67-\delta}(Al, Si,Fe^{3+})_{2+\delta}O_4$, implying that cation disorder between B and C cations takes place, which was also suggested by Gasparik et al. (2000).

3.3. Volume fractions of phases and density of the MORB system

Fig. 7 shows the volume fractions of phases in MORB calculated from a mass balance of the present chemical composition data. The volume fraction of Brg gradually increases from 25 to 33 vol.% with increasing pressure, becoming the most abundant mineral in the MORB system in the mid-mantle. The NAL fraction is limited up to 2 vol.%, which agrees with values reported by Ishii et al. (2019a) up to 28 GPa, and does not change significantly up to 52 GPa. Although NAL and CF have very similar chemical compositions, NAL is K-rich owing to its large space structure that can accommodate relatively large ions compared with CF. The limited and constant amounts of NAL in the MORB system indicate that NAL is stabilized only as a K host. Perrillat et al. (2006) and Ricolleau et al. (2010) reported that 10-20 vol.% of NAL in the MORB system up to ~50 GPa. The Soret effect caused by the steep temperature gradient induced by the laser heating should have produced different phase assemblages from the MORB system in their samples, making NAL either more stable or formed as a metastable phase during the syntheses. In fact, NAL in Ricolleau et al. (2010) does not contain any K, which may imply that the bulk composition after the laser heating is significantly different from ours. The volume frac-

tions of CF, St, and Dm are 20-25 vol.%, which slightly decrease with pressure concurrently with the increase of bridgmanite.

Fig. 8 shows the density evolution of the MORB system as a function of pressure at 1700, 2000, and 2300 K. The density at 2000 K is by ~2-3% higher than peridotite between 27 GPa and 52 GPa, which is consistent with the previous studies (Perrillat et al., 2006; Ricolleau et al., 2010). The difference seems to gradually increase from +2% at 27 GPa with increasing pressure and reach +3% at 52 GPa. Temperature variations of ±300 K cause a density change of only ±0.5%. Thus, our results support a previous conclusion that the MORB system is denser than peridotite systems under mid-mantle conditions (Perrillat et al., 2006; Ricolleau et al., 2010).

3.4. Implications for lower-mantle structure and dynamics

Basaltic Brg has significant amounts of the oxygen vacancy component (~11%) compared to peridotitic Brg (2-3%) (Frost et al., 2004; Irifune et al., 2010), which disappear around 40 GPa, corresponding to a 1000 km depth. Seismic tomography images showed that many subducting slabs stagnate between 660 and 1000 km depths (Fukao and Obayashi, 2013). Basaltic fragments from the stagnated slabs in the lower mantle may cause a viscosity change from 660 to 1000 km depth (Rudolph et al., 2015) because basaltic Brg, having a large amount of oxygen vacancy up to ~1000 km depth, can be much softer than peridotitic oxygen-vacancy-free Brg (Reali et al., 2019). This viscosity change can explain slab stagnation at ~1000 km depth. Previous studies also suggest that basaltic crust may especially remain in the mid-mantle compared with the upper part of the lower mantle (Jenkins et al., 2017; Bentham et al., 2017). This concentration of basaltic crust may be due to the segregation of basaltic crust from the subducting slab around 1000 km depth by the disappearance of oxygen vacancy component and therefore the subsequent hardening of bridgmanite.

Seismic tomography images also showed the invisibility or smearing of upwelling hot plumes between 660 and 1000 km depths. This phenomenon can also be explained by the change in the chemistry of basaltic Brg. Li et al. (2014) suggested that basaltic crust materials subducted into the lower mantle are entrained into upwelling hot plumes. Basaltic Brg in hot plumes from the bottom of the lower mantle can have lower viscosity below 1000 km depth due to the low concentration of oxygen vacancy components below 1000 km depth. This will reduce the viscosity of plumes and therefore accelerate their upwelling in combination with a viscosity change in the ambient mantle, causing the invisibility or smearing.

Large low-shear-velocity provinces (LLSVPs) beneath the Pacific and African plates are another debated topic concerning the structure and dynamics of the lower mantle. Seismological and geochemical observations show that these regions has higher density but lower shear-wave velocity than the ambient mantle with sharp boundaries at the edge (Garnero et al., 2016). Geochemical data also suggest that subducted basaltic crusts are a plausible candidate to explain the origin of LLSVPs (Niu, 2018). Recent high-pressure experimental data showed that Dm has significantly low shear- and compressional-wave velocities, suggesting the presence of MORB in LLSVPs (Thomson et al., 2019). However, their estimation was based on the extrapolation of the low-pressure (~12 GPa) data, and therefore needs to be verified using higher-pressure data. The present work showed that basaltic Brg is Fe^{2+}-enriched (Fig. 5b). Experimental studies suggest that $Fe^{2+}SiO_3$-enriched Brg has higher bulk sound velocity and lower shear-wave velocity (Mao et al., 2011; Mashino et al., 2020), although the combined effect of other components such as $FeAlO_3$ and Al_2O_3 is still unclear. Further sound velocity measurements on Fe^{2+}-rich bridgmanite will provide a better constraint on the structure of LLSVPs.

4. Conclusion

We have determined phase relations of MORB down to mid-mantle conditions (27-52 GPa at 2000 K, corresponding to 740-1300 km depths) using a multi-anvil press in combination with post-analyses using synchrotron XRD and TEM with EDS and EELS on the quenched samples. Our findings are as follows.

(1) All run products consist of the five phases of Brg, St, Dm, CF, and NAL.

(2) The fraction of NAL depends on the bulk potassium content, and therefore is very limited (up to 2 vol.%) in the MORB system.

(3) The ferric iron ratios to the total iron in MORB Brg are only 14-28 %, which is in striking contrast with peridotitic Brg (∼70%).

(4) Ferric iron is strongly partitioned into NAL, whereas ferrous iron is preferably incorporated in Brg and CF.

(5) The incorporation of ferric iron in Brg, CF, and NAL implies that they cause iron disproportionation in MORB layers of subducted slabs.

(6) Brg has a significant oxygen vacancy component of $MgAlO_{2.5}$ (∼11 mol.%) below 40 GPa, which is much higher than that in peridotitic Brg (2-3 mol.%) and disappears above 40 GPa.

(7) The $FeAlO_3$ component is minor in basaltic Brg and decreases with increasing pressure.

These findings implicate the lower mantle structure and dynamics. If significant amounts of subducted MORB accumulate in the lower mantle, the MORB component may affect the mantle viscosity change observed between 660 and 1000 km depths because the rapid decrease in oxygen vacancy in basaltic Brg with depth should increase the viscosity. If MORB is subducted to the bottom of the lower mantle, the low ferric iron ratio in basaltic Brg can support the previous hypothesis that large low-shear-velocity provinces (LLSVPs) are formed by subducted MORB because Fe^{2+}-rich Brg may show low shear-wave velocity compared to Fe^{3+}-rich one.

CRediT authorship contribution statement

Takayuki Ishii: Conceptualization, Formal analysis, Funding acquisition, Investigation, Methodology, Project administration, Validation, Visualization, Writing – original draft. **Nobuyoshi Miyajima:** Formal analysis, Funding acquisition, Investigation, Writing – review & editing. **Giacomo Criniti:** Formal analysis, Investigation, Writing – review & editing. **Qingyang Hu:** Investigation, Resources, Writing – review & editing. **Konstantin Glazyrin:** Investigation, Writing – review & editing. **Tomoo Katsura:** Conceptualization, Funding acquisition, Writing – review & editing.

Declaration of competing interest

The authors declare that they have no competing interests or personal relationships that could have appeared to influence the work reported in this paper.

Acknowledgements

Appendix A. Supplementary material

Supplementary material related to this article can be found online at https://doi.org/10.1016/j.epsl.2022.117472.

References

Ballmer, M.D., Schmerr, N.C., Nakagawa, T., Ritsema, J., 2015. Compositional mantle layering revealed by slab stagnation at ∼1000-km depth. Sci. Adv. 1, e1500815.

Bentham, H.L.M., Rost, S., Thorne, M.S., 2017. Fine-scale structure of the mid-mantle characterised by global stacks of PP precursors. Earth Planet. Sci. Lett. 472, 164–173.

Bérar, J.F., Lelann, P., 1991. E.S.D.'s and estimated probable error obtained in rietveld refinements with local correlations. J. Appl. Crystallogr. 24, 1–5.

Dziewonski, A.M., Anderson, D.L., 1981. Preliminary Reference Earth Model (PREM). Phys. Earth Planet. Inter. 25, 297–356.

Frost, D.J., Liebske, C., Langenhorst, F., McCammon, C.A., Trønnes, R.G., Rubie, D.C., 2004. Experimental evidence for the existence of iron-rich metal in the arth's lower mantle. Nature 428, 409–412.

Fukao, Y., Obayashi, M., 2013. Subducted slabs stagnant above, penetrating through, and trapped below the 660 km discontinuity. J. Geophys. Res., Solid Earth 118, 5920–5938.

Garnero, E.J., McNamara, A.K., Shim, S.H., 2016. Continent-sized anomalous zones with low seismic velocity at the base of Earth's mantle. Nat. Geosci. 9, 481–489.

Gasparik, T., Tripathi, A., Parise, J.B., 2000. Structure of a new Al-rich phase, $[K,Na]_{0.9}[Mg, Fe]_2[Mg, Fe,Al, Si]_6O_{12}$, synthesized at 24 GPa. Am. Mineral. 85, 613–618.

Gréaux, S., Irifune, T., Higo, Y., Tange, Y., Arimoto, T., Liu, Z., Yamada, A., 2019. Sound velocity of $CaSiO_3$ perovskite suggests the presence of basaltic crust in the Earth's lower mantle. Nature 565, 218–221.

Hirose, K., Fei, Y., Ma, Y., Mao, H.K., 1999. The fate of subducted basaltic crust in the Earth's lower mantle. Nature 397, 53–56.

Hirose, K., Fei, Y., 2002. Subsolidus and melting phase relations of basaltic composition in the uppermostlower mantle. Geochim. Cosmochim. Acta 66, 2099–2108.

Hirose, K., Takafuji, N., Sata, N., Ohishi, Y., 2005. Phase transition and density of subducted MORB crust in the lower mantle. Earth Planet. Sci. Lett. 237, 239–251.

Huang, R., Ballaran, T.B., McCammon, C.A., Miyajima, N., Dolejš, D., Frost, D.J., 2021. The composition and redox state of bridgmanite in the lower mantle as a function of oxygen fugacity. Geochim. Cosmochim. Acta 303, 110–136.

Irifune, T., Ringwood, A.E., 1993. Phase transformations in subducted oceanic crust and buoyancy relationships at depths of 600–800 km in the mantle. Earth Planet. Sci. Lett. 117, 101–110.

Irifune, T., Shinmei, T., McCammon, C.A., Miyajima, N., Rubie, D.C., Frost, D.J., 2010. Iron partitioning and density changes of pyrolite in earth's lower mantle. Science 327, 193–195.

Ishii, T., Shi, L., Huang, R., Tsujino, N., Druzhbin, D., Myhill, R., Li, Y., Lin, W., Yamamoto, T., Miyajima, N., Kawazoe, T., Nishiyama, N., Higo, Y., Tange, Y., Katsura, T., 2016. Generation of pressures over 40 GPa using Kawai-type multi-anvil press with tungsten carbide anvils. Rev. Sci. Instrum. 87, 024501.

Ishii, T., Yamazaki, D., Tsujino, N., Xu, F., Liu, Z., Kawazoe, T., Yamamoto, T., Druzhbin, D., Wang, L., Higo, Y., Tange, Y., Yoshino, T., Katsura, T., 2017. Pressure generation to 65 GPa in a Kawai-type multi-anvil apparatus with tungsten carbide anvils. High Press. Res. 37, 507–515.

Ishii, T., Kojitani, H., Akaogi, M., 2019a. Phase relations of Harzburgite and MORB up to the uppermost lower mantle conditions: Precise comparison with Pyrolite by multisample cell high-pressure experiments with implication to dynamics of subducted slabs. J. Geophys. Res., Solid Earth 124, 3491–3507.

Ishii, T., Liu, Z., Katsura, T., 2019b. A breakthrough in pressure generation by a Kawai-type multi-anvil apparatus with Tungsten Carbide Anvils. Engineering 5, 434–440.

Jenkins, J., Deuss, A., Cottaar, S., 2017. Converted phases from sharp 1000 km depth mid-mantle heterogeneity beneath Western Europe. Earth Planet. Sci. Lett. 459, 196–207.

Kaneshima, S., 2019. Seismic scatterers in the lower mantle near subduction zones. Geophys. J. Int. 219, S2–S20.

Kurnosov, A., Marquardt, H., Frost, D.J., Ballaran, T.B., Ziberna, L., 2017. Evidence for a Fe^{3+}-rich pyrolitic lower mantle from (Al, Fe)-bearing bridgmanite elasticity data. Nature 543, 543–546.

Lakshtanov, D.L., Sinogeikin, S.V., Litasov, K.D., Prakapenka, V.B., Hellwig, H., Wang, J., Sanches-Valle, C., Perrillat, J.-P., Chen, B., Somayazulu, M., Li, J., Ohtani, E., Bass, J.D., 2007. The post-stishovite phase transition in hydrous alumina-bearing SiO_2 in the lower mantle of the earth. Proc. Natl. Acad. Sci. 104, 13588–13590.

Li, M., McNamara, A.K., Garnero, E.J., 2014. Chemical complexity of hotspots caused by cycling oceanic crust through mantle reservoirs. Nat. Geosci. 7, 366–370.

Litasov, K.D., Ohtani, E., 2005. Phase relations in hydrous MORB at 18–28 GPa: implications for heterogeneity of the lower mantle. Phys. Earth Planet. Inter. 150, 239–263.

Liu, Z., Nishi, M., Ishii, T., Fei, H., Miyajima, N., Ballaran, T.B., Ohfuji, H., Sakai, T., Wang, L., Shcheka, S., Arimoto, T., Tange, Y., Higo, Y., Irifune, T., Katsura, T., 2017a. Phase relations in the system $MgSiO_3$-Al_2O_3 up to 2300 K at lower mantle pressures. J. Geophys. Res., Solid Earth 122, 7775–7788.

Liu, Z., Ishii, T., Katsura, T., 2017b. Rapid decrease of $MgAlO_{2.5}$ component in bridgmanite with pressure. Geochem. Perspect. Lett. 5, 12–18.

Liu, Z.D., Ballaran, T.B., Huang, R., Frost, D.J., Katsura, T., 2019. Strong correlation of oxygen vacancies in bridgmanite with Mg/Si ratio. Earth Planet. Sci. Lett. 523, 115697.

Liu, Z., McCammon, C., Wang, B., Dubrovinsky, L., Ishii, T., Bondar, D., Nakajima, A., Tange, Y., Higo, Y., Cui, T., Liu, B., Katsura, T., 2020. Stability and solubility of the $FeAlO_3$ component in bridgmanite at uppermost lower mantle conditions. J. Geophys. Res., Solid Earth 125, e2019JB018447.

Mao, Z., Lin, J.F., Scott, H.P., Watson, H.C., Prakapenka, V.B., Xiao, Y., Chow, P., McCammon, C., 2011. Iron-rich perovskite in the Earth's lower mantle. Earth Planet. Sci. Lett. 309, 179–184.

Mashino, I., Murakami, M., Miyajima, N., Petitgirard, S., 2020. Experimental evidence for silica-enriched Earth's lower mantle with ferrous iron dominant bridgmanite. Proc. Natl. Acad. Sci. 117 (45), 27899–27905.

Miyajima, N., Fujino, K., Funamori, N., Kondo, T., Yagi, T., 1999. Garnet-perovskite transformation under conditions of the Earth's lower mantle: an analytical transmission electron microscopy study. Phys. Earth Planet. Inter. 116, 117–131.

Miyajima, N., Yagi, T., Hirose, K., Kondo, T., Fujino, K., Miura, H., 2001. Potential host phase of aluminum and potassium in the Earth's lower mantle. Am. Mineral. 86, 740–746.

Miyajima, N., Langenhorst, F., Frost, D.J., Yagi, T., 2004. Electron channeling spectroscopy of iron in majoritic garnet and silicate perovskite using a transmission electron microscope. Phys. Earth Planet. Inter. 143–144, 601–609.

Nishihara, Y., Nakayama, K., Takahashi, E., Iguchi, T., Funakoshi, K.I., 2005. P-V-T equation of state of stishovite to the mantle transition zone conditions. Phys. Chem. Miner. 31, 660–670.

Niu, Y., 2018. Origin of the LLSVPs at the base of the mantle is a consequence of plate tectonics–a petrological and geochemical perspective. Geosci. Front. 9, 1265–1278.

Ono, S., Yasuda, A., 1996. Compositional change of majoritic garnet in a MORB composition from 7 to 17 GPa and 1400 to 1600 °C. Phys. Earth Planet. Inter. 96, 171–179.

Ono, S., Ito, E., Katsura, T., 2001. Mineralogy of subducted basaltic crust (MORB) from 25 to 37 GPa, and chemical heterogeneity of the lower mantle. Earth Planet. Sci. Lett. 190, 57–63.

Ono, S., Hirose, K., Isshiki, M., Mibe, K., Saito, Y., 2002. Equation of state of hexagonal aluminous phase in basaltic composition to 63 GPa at 300 K. Phys. Chem. Miner. 29, 527–531.

Perrillat, J.P., Ricolleau, A., Daniel, I., Fiquet, G., Mezouar, M., Guignot, N., Cardon, H., 2006. Phase transformations of subducted basaltic crust in the upmost lower mantle. Phys. Earth Planet. Inter. 157, 139–149.

Petříček, V., Dušek, M., Palatinus, L., 2014. Crystallographic computing system JANA2006: general features. Z. Kristallogr. 229, 345–352.

Piet, H., Badro, J., Nabiei, F., Dennenwaldt, T., Shim, S.H., Cantoni, M., Hébert, C., Gillet, P., 2016. Spin and valence dependence of iron partitioning in Earth's deep mantle. Proc. Natl. Acad. Sci. 113, 11127–11130.

Prescher, C., Langenhorst, F., Dubrovinsky, L.S., Prakapenka, V.B., Miyajima, N., 2014. The effect of Fe spin crossovers on its partitioning behavior and oxidation state in a pyrolitic Earth's lower mantle system. Earth Planet. Sci. Lett. 399, 86–91.

Prescher, C., Prakapenka, V.B., 2015. DIOPTAS: a program for reduction of two-dimensional X-ray diffraction data and data exploration. High Press. Res. 5, 223–230.

Reali, R., Van Orman, J.A., Pigott, J.S., Jackson, J.M., Boioli, F., Carrez, P., Cordier, P., 2019. The role of diffusion-driven pure climb creep on the rheology of bridgmanite under lower mantle conditions. Sci. Rep. 9, 1–9.

Ricolleau, A., Perrillat, J.P., Fiquet, G., Daniel, I., Matas, J., Addad, A., Menguy, N., Cardon, H., Mezouar, M., Guignot, N., 2010. Phase relations and equation of state of a natural MORB: implications for the density profile of subducted oceanic crust in the Earth's lower mantle. J. Geophys. Res., Solid Earth 115, B08202.

Rudolph, M.L., Lekić, V., Lithgow-Bertelloni, C., 2015. Viscosity jump in Earth's mid-mantle. Science 350, 1349–1352.

Shinmei, T., Sanehira, T., Yamazaki, D., Inoue, T., Irifune, T., Funakoshi, K.I., Nozawa, A., 2005. High-temperature and high-pressure equation of state for the hexagonal phase in the system $NaAlSiO_4$-$MgAl_2O_4$. Phys. Chem. Miner. 32, 594–602.

Sinmyo, R., Hirose, K., Muto, S., Ohishi, Y., Yasuhara, A., 2011. The valence state and partitioning of iron in the Earth's lowermost mantle. J. Geophys. Res., Solid Earth 116, B07205.

Thomson, A.R., Crichton, W.A., Brodholt, J.P., Wood, I.G., Siersch, N.C., Muir, J.M.R., Dobson, D.P., Hunt, S.A., 2019. Seismic velocities of $CaSiO_3$ perovskite can explain LLSVPs in Earth's lower mantle. Nature 572, 643–647.

Tschauner, O., Huang, S., Yang, S., Humayun, M., 2020. Davemaoite, IMA 2020-012a. CNMNC Newsletter No. 58. Mineral. Mag. 84. https://doi.org/10.1180/mgm.2020.93.

van Aken, P., Liebscher, B., 2002. Quantification of ferrous/ferric ratios in minerals: new evaluation schemes of Fe L_{23} electron energy-loss near-edge spectra. Phys. Chem. Miner. 29, 188–200. https://doi.org/10.1007/s00269-001-0222-6.